Draft version October 23, 2026
Typeset using LaTeX **twocolumn** style in AASTeX631

arXiv:2512.01492v2 [astro-ph.SR] 22 Oct 2026

Velocity-space turbulent cascade in the near-Sun solar wind: first insights from the Parker Solar Probe mission

A. Larosa [1], O. Pezzi [1], T. Bowen [2,3], L. Sorriso-Valvo [1,4], N. Sioulas [2,3], F. Pucci [1], D. Trotta [5], J. L. Verniero [6], R. Livi [2,3], S. Bharati Das [7], A. Chasapis [8], D. Perrone [9], F. Valentini [10] and S. Servidio [10]

[1] *Istituto per la Scienza e Tecnologia dei Plasmi (ISTP), Consiglio Nazionale delle Ricerche, I-70126 Bari, Italy*
[2] *University of California, Berkeley, CA, USA*
[3] *Space Sciences Laboratory, University of California, Berkeley, CA 94720-7450, USA*
[4] *Space and Plasma Physics, School of Electrical Engineering and Computer Science, KTH Royal Institute of Technology, 11428, Stockholm, Sweden*
[5] *European Space Agency (ESA), European Space Astronomy Centre (ESAC), Camino Bajo del Castillo s/n, 28692 Villanueva de la Cañada, Madrid, Spain*
[6] *Heliophysics Science Division, NASA Goddard Space Flight Center, Greenbelt, MD 20771, USA*
[7] *Center for Astrophysics — Harvard & Smithsonian, 60 Garden Street, Cambridge, MA 02138, USA.*
[8] *Laboratory of Atmospheric and Space Physics, University of Colorado, Boulder, CO 80303, USA*
[9] *ASI – Italian Space Agency, via del Politecnico snc, I-00133 Rome, Italy*
[10] *Dipartimento di Fisica, Universita' della Calabria, I-87036 Rende (CS), Italy*

ABSTRACT

In space plasmas, the rarity of collisions leads to complex structures in the velocity space where a turbulent cascade of the velocity distribution function fluctuations is thought to occur. Previous studies have explored this phenomenon using the Hermite decomposition of the ion velocity distribution function (VDF) in both magnetosheath data and numerical simulations. In this work, we investigate the Hermite spectrum of the ion VDFs measured by Parker Solar Probe in the inner heliosphere. We analyze a superalfvénic stream at a radial distances of $R \approx 28R_{sun}$ and a subalfvénic at $R \approx 11R_{sun}$, the former characterized by a prevalence of VDFs with suprathermal beams (also known as hammerhead). The Hermite analysis is also compared with various proxies of energization and dissipation, in order to establish a connection between turbulent cascades in real space and those in the velocity space. A qualitative agreement between the energization proxies and the Hermite analysis is observed. The results are suggestive of the presence of a dual cascade in real and velocity space.

Keywords: heliosphere — solar wind — turbulence

1. INTRODUCTION

Nearly-collisionless turbulent space plasmas, such as the solar wind and Earth's magnetosheath, are usually far from the local thermodynamical equilibrium (LTE) (Bruno & Carbone 2013; Cassak et al. 2023). Energy conversion and dissipation influence the entire six-dimensional phase space, and plasma velocity distribution functions (VDFs) are typically characterized by distinct non-Maxwellian structures, including temperature anisotropy, beams, rings, and finer-scale non-thermal velocity-space distortions. The generation of finer and finer scale non-equilibrium structures in the VDF has often been envisioned as a turbulent cascade process in velocity space, where the cascading quantities are enstrophy and entropy (Schekochihin et al. 2008; Tatsuno et al. 2009; Schekochihin et al. 2016; Servidio et al. 2017). Such a cascade is considered to be an avenue towards irreversible heating in plasmas with an extremely small collisional frequency.

Recently, numerical works (Cerri et al. 2018; Pezzi et al. 2018, 2019; Cerri et al. 2021; Celebre et al. 2023; Nastac et al. 2024) and observation studies in the near-Earth solar wind and in Earth's magnetosheath (Servidio et al. 2017; Wu et al. 2023) have further explored this concept, while it still remains relatively unexplored in laboratory plasmas (Howes 2018) and in the inner heliosphere, mainly due to the lack of data. However, thanks to the NASA spacecraft Parker Solar Probe (PSP) (Fox et al. 2016; Raouafi et al. 2023), it has been possible to have a privileged observational point of a

completely unexplored environment. PSP data have revealed, in the near-Sun solar wind, unprecedented complexity of the VDFs, which often exhibit the so-called "hammerhead" shape (Verniero et al. 2020, 2022).

A meaningful way to quantify this complexity is through the Hermite decompositions of the VDFs. The Hermite transform, which is a series expansion of the VDF in term of a Maxwellian weighted by Hermite polynomials, relates to a Maxwellian just as the Fourier transform relates to a plane wave: a single Fourier mode describes a plane wave, and likewise a single Hermite mode describes a Maxwellian. The more Hermite modes are non-zero the more the VDF is far from a Maxwellian.

This method has been used to investigate the phase space cascade in the magnetosheath (Servidio et al. 2017), in solar wind reconnection exhausts (Wu et al. 2023), and in Vlasov-Maxwell numerical simulations exploring different turbulent fluctuations amplitude and plasma β conditions (Pezzi et al. 2018; Cerri et al. 2018). Different heating mechanism have different velocity space signatures (Huang et al. 2024) whose dominance strongly depends on the plasma, kinetic to magnetic pressure ratio, β (Cerri et al. 2021; Huang et al. 2024). Therefore, it is crucial to understand if and how the velocity-space turbulent cascade also depends on β.

The Hermite or Hermite-Laguerre transform also provides a nonparametric and analytical representation of the VDFs, which enables one to compute VDF derivatives, necessary to study wave-particle interactions (Bowen et al. 2022; Coburn et al. 2024).

Moreover, the exponent of the power-law Hermite spectrum might be informative about the dominant physical process that controls the cascade. According to a Kolmogorov-like phenomenology, a -1.5 exponent is expected for a phase-mixing or electric-field-dominated regime, while a -2 exponent indicates a magnetic-field-dominated regime (Servidio et al. 2017). Furthermore, the exponent has been shown to be affected by the competition of linear against nonlinear processes, with a steeper spectrum in the nonlinear-dominated regime in electrostatic ion-temperature-gradient driven drift-kinetic turbulence (Parker et al. 2016), while in Vlasov-Poisson systems power-laws are observed when instabilities or turbulence are present, but not in linear regimes (Celebre et al. 2023).

The study of the phase space cascade through the Hermite spectrum can be complemented by inspecting different measures of energy conversion and dissipation, which can be based either on the energy in the fields or on the VDF. This is crucial in order to link the velocity-space complexity with the turbulent cascade. Indeed, the existence of a cascade in the phase space and its relation to turbulent fluctuations are crucial elements towards the understanding of how nearly collisionless plasmas are heated in a thermodynamic (irreversible) sense (Schekochihin et al. 2008; Tatsuno et al. 2009; Pezzi et al. 2016; Nastac et al. 2024).

In this work, we explore this link through a study of the phase-space cascade using PSP measurements in the inner heliosphere. In particular, we focus on a proxy for local turbulent energy transfer (LET) (Sorriso-Valvo et al. 2019) and on a quantitative measure of the deviation of the VDFs from Maxwellianity (Kaufmann & Paterson 2009a; Liang et al. 2020). Although these measures do not distinguish between different physical processes, they are capable of locating regions of strong dissipation and non-linear energy transfer that should also be captured in the Hermite analysis of the VDFs. An extensive review of these quantities is given in Pezzi et al. (2021).

Data and methods are described in Section 2, the properties of the streams under investigation and their Hermite spectra in Section 3, and the link between VDF and fields-based proxies for dissipation and energization in Section 4. We conclude in Section 5.

2. DATA AND METHODS

We use data from the FIELDS (Bale et al. 2016) and SWEAP (Kasper et al. 2016) instrument suites onboard PSP. FIELDS provides the magnetic field data from both the flux-gate magnetometer and the search coil magnetometer (Jannet et al. 2021; Dudok de Wit et al. 2022). These two data products are combined in the SCaM dataset (Bowen et al. 2020a) that has an excellent signal-to-noise ratio. Unfortunately, due to an anomaly, only two components of the search coil magnetometer magnetic field are available past the first encounter (Dudok de Wit et al. 2022).

The SWEAP sensors provide the electron pitch-angle distribution (ePAD) from the SPAN-e instrument (Whittlesey et al. 2020) and the proton velocity distribution functions and their moments from the SPAN-i instrument (Livi et al. 2022). The ePAD is used to select intervals with a unidirectional electron strahl in order to exclude complex magnetic topologies from the analysis (see Owens & Forsyth 2013, for the connections between the strahl and the magnetic topology), that could invalidate the interpretation of the time averages as ensemble averages.

In this work we use SPAN-i data from encounters 4 and 18, whose respective cadence is 7 and 1.7 seconds corresponding to about 13 and 21 cyclotron times, being the ion cyclotron frequency $\Omega_{cp} = eB/m_pc$ computed with the average magnetic field for each interval.

SPAN-i VDFs have a three-dimensional (3D) resolution in velocity space of $8 \times 32 \times 8$ in azimuth, energy and elevation, respectively. For each bin of the SPAN-i instrument grid, we move from the instrument grid to the field-aligned coordinates ($v_\parallel$, $v_{\perp 1}$, $v_{\perp 2}$), where $v_\parallel$ is along the local magnetic field and $v_{\perp 1}$ and $v_{\perp 2}$ are orthogonal to it. The local magnetic field used is the one at the SPAN-i cadence available in the L3 SPAN-i data products.

Then, we define $v_\perp = \sqrt{v_{\perp 1}^2 + v_{\perp 2}^2}$, thus assuming gyrotropy (as in Bowen et al. 2022) in the directions perpendicular to the local field. Hence, we reduce the VDF to a two-dimensional (2D) velocity-space in $v_\parallel$ and $v_\perp$.

The Hermite decomposition requires defining the velocity domain in $(-\infty, \infty)$. Therefore, following Bowen et al. (2022), we impose $f(-v_\perp) = f(v_\perp)$ and extend the grid to negative values in the perpendicular direction consistently with the gyrotropy assumption (see Appendix A to visualize the effect of this approach on the VDFs). Note that such a procedure implies null odd Hermite coefficients in the perpendicular direction.

We shift the velocity grids, in both parallel and perpendicular directions, such that the bulk speed is zero. Moreover, the velocity grids are normalized by their respective (perpendicular and parallel) thermal speeds. The shift and the normalization ensure that fluctuations in the 1$^{\text{st}}$ and 2$^{\text{nd}}$ order VDF moments, associated with bulk flows or large-scale energy conversion (e.g., due to radial expansion) do not influence the Hermite spectrum at high modes (Pezzi et al. 2018).

The Hermite decomposition of a VDF, at a given instant in time, is hence defined as:

$$f(v_\perp, v_\parallel) = \sum_{m_\perp, m_\parallel} g_{m_\perp, m_\parallel}\, \psi_{m_\perp}(\xi_\perp)\, \psi_{m_\parallel}(\xi_\parallel), \qquad (1)$$

where the normalized velocity coordinates are $\xi_\perp = (v_\perp - u_\perp)/v_{\text{th},\perp}$ and $\xi_\parallel = (v_\parallel - u_\parallel)/v_{\text{th},\parallel}$, being u and v_{th} respectively the bulk velocity and the thermal speed in each direction. The orthonormal Hermite eigenfunctions are

$$\psi_m(\xi) = \frac{H_m(\xi)}{\sqrt{2^m \sqrt{\pi} m!}} e^{-\frac{\xi^2}{2}}, \qquad (2)$$

where $H_m(\xi)$ are the physicist's Hermite polynomials

$$H_m(\xi) = (-1)^m e^{\xi^2} \frac{d^m}{d\xi^m} e^{-\xi^2}, \qquad (3)$$

and $m = m_\perp, m_\parallel$. By exploiting the orthonormality condition $\int_{-\infty}^{\infty} d\xi \psi_m(\xi)\psi_n(\xi) = \delta_{m,n}$, the Hermite coefficient $g_{m_\perp, m_\parallel}$ can be calculated as:

$$g_{m_\perp, m_\parallel} = \int_{-\infty}^{\infty}\int_{-\infty}^{\infty} f(v_\perp, v_\parallel)\, \psi_{m_\perp}(\xi_\perp)\, \psi_{m_\parallel}(\xi_\parallel)\, d\xi_\perp\, d\xi_\parallel. \qquad (4)$$

As discussed by Servidio et al. (2017) and Pezzi et al. (2018), each VDF is interpolated on the 2D quadrature grid corresponding to the roots of the $N_v + 1$-th Hermite polynomials before computing the coefficients $g_{m_\perp, m_\parallel}$, being N_v the maximum order of Hermite polynomials in each direction. This procedure allows us to exploit the Gauss-Hermite quadrature to compute integrals and, in particular, the Parseval-Plancerel spectral theorem, $\int f^2 d\xi_\perp\, d\xi_\parallel = \sum g^2_{m_\perp, m_\parallel}$, which connects the enstrophy with the sum of Hermite coefficients squared. The one-dimensional Hermite spectrum $P(m)$ is then computed over concentric-shells of unit thickness in the Hermite space, i. e. $P(m) = \sum_{m-1/2<|\mathbf{m}'|\leq m+1/2} g^2_{\mathbf{m}'}$ where $m = \sqrt{m_\perp^2 + m_\parallel^2}$ and $\mathbf{m} = (m_\perp, m_\parallel)$. For this work, we choose $N_v = 50$ such that the number of Hermite grid points ($50^2 = 2500$) is close to the number of instrument grid points ($8 \times 32 \times 8 = 2048$). We note that in general shell averaging the spectra could cause the mixture of high and low m modes if the parallel and perpendicular thermal speed are very different, therefore using the trace speed should also be considered. However, we verified that for the streams studied here using the trace speed does not modify significantly the spectra.

3. STREAMS PROPERTIES AND HERMITE SPECTRA

We investigate the properties of two different intervals, hereafter identified as the *wave stream* (Figure 1, top) and the *turbulent stream* (Figure 1, bottom). Figure 1 shows, from top to bottom, the magnetic field components, the velocity components, proton density and parallel and perpendicular temperatures and the spectrogram of the magnetic helicity for the two streams. The magnetic helicity is defined as

$$\sigma_m = \frac{2\Im\left(\tilde{B_T^\star} \tilde{B_N}\right)}{|\tilde{B_R}|^2 + |\tilde{B_T}|^2 + |\tilde{B_N}|^2}, \qquad (5)$$

where B indicates the magnetic field components, the $\tilde{}$ represents the wavelet- transformed quantities and $\star$ represents the operation complex conjugation (Matthaeus et al. 1982). We use a Morlet wavelet.

The streams are chosen in order to have a mostly radial magnetic field in order to avoid field of view issue with SPAN-i (see Livi et al. 2022). The average properties are listed in Table 1. The superalfvénic *wave stream*

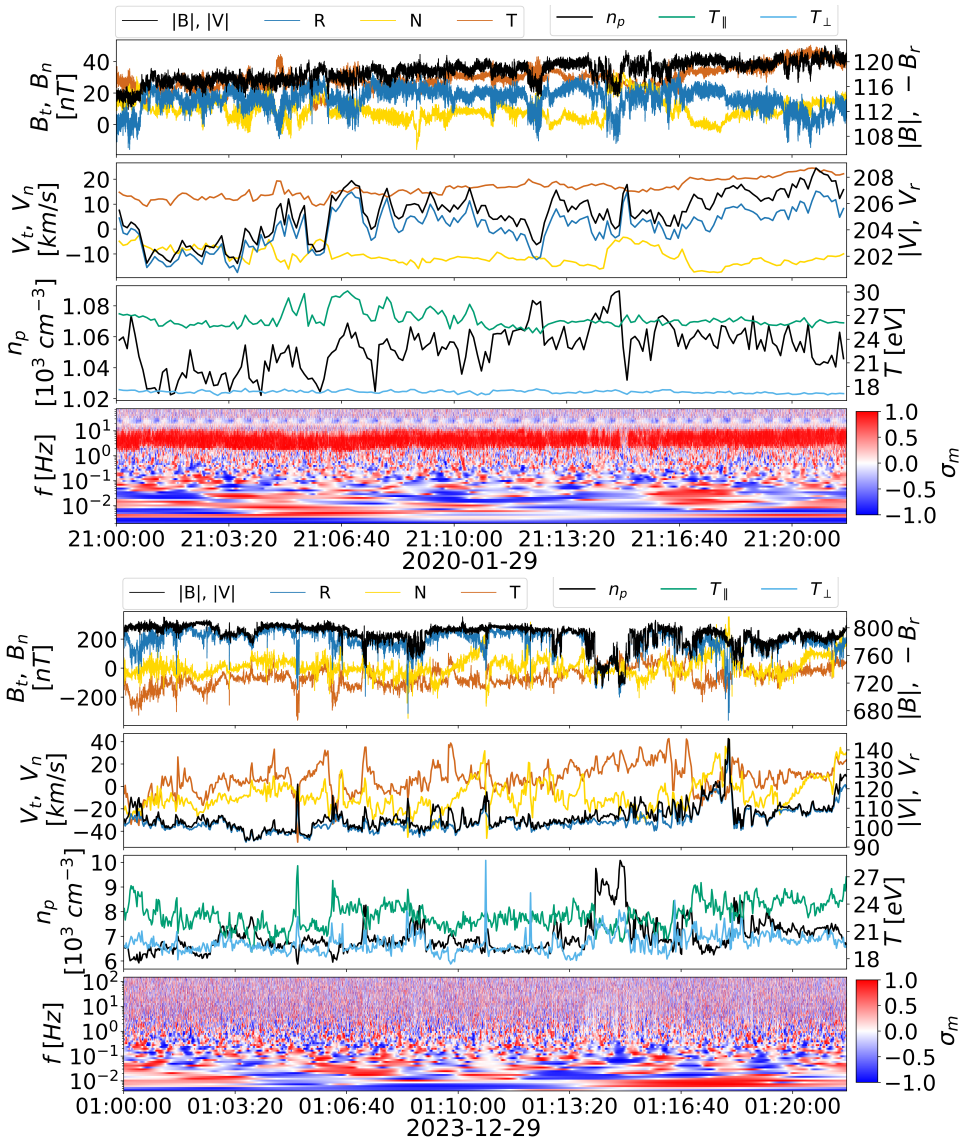


Figure 1. Magnetic field, velocity field, density and parallel and perpendicular temperatures and magnetic helicity in the *wave stream* (top) and *turbulent stream* (bottom).

was measured on 2020 January 29 from 21:00 to 21:21:37 UTC and the subalfvénic *turbulent stream* on 2023 December 29 from 01:00 to 01:21:37 UTC.

Quantity	*wave*	*turbulent*
$B_{\rm rms}$ $[nT]$	9.83	95.81
$B_{\rm rms}/\langle B\rangle$	0.08	0.12
$\langle\beta_p\rangle$	0.6	0.1
$\langle\theta_{BV}\rangle^\circ$	168	116
$\langle\sigma_c\rangle$	0.69	0.79
R $[R_{sun}]$	28.0	11.4
M_A	2.6	0.5
f_c $[Hz]$	1.8	12

Table 1. Summary of streams average properties.

Both intervals are characterized by a mostly radial magnetic field and are highly Alfvénic and unbalanced, with high normalized cross-helicity σ_c, see Table 1. The rms fluctuation level and the density are one order of magnitude stronger for the *turbulent stream* closer to the Sun, but the ratio $B_{\rm rms}/\langle B\rangle$ is of the same order for both intervals. $\langle B\rangle$ is the magnitude of the mean of the magnetic field over the full interval. The average proton kinetic to magnetic pressure ratio $\beta_p = \frac{nk_BT_p}{B^2/2\mu_0}$ is smaller for the *turbulent stream*.

The two streams have a different average angle between the magnetic field and the velocity, θ_{BV}. The *wave stream* has almost antiparallel sampling ($\theta_{BV} = 168^\circ$), while the *turbulent stream* has more perpendicular sampling ($\theta_{BV} = 116^\circ$). The angle is computed

in the spacecraft frame to take into account the large tangential velocity of PSP which affect the sampling direction (e.g. Klein et al. 2015). This explains why, even though both the plasma velocity and the magnetic field are mostly along the radial direction (see Fig.1) we can have large θ_{BV}.

Two representative VDFs for the two streams are shown in Figure 2. For both streams the SPAN-I sensor has a good field of view, with the core of the distribution being always mostly resolved. PSP observations have shown the prevalence of VDFs with large proton beams that undergo perpendicular velocity-space diffusion at higher energies, resembling a "hammerhead" shape (Verniero et al. 2020, 2022) (hereby referred to as hammerhead distributions). This is exemplified in Figure 2 (top), where the beam at larger $v_{\parallel}$ spreads to larger $v_{\perp}$. Hammerhead distributions are dominant in the *wave stream*, which present parallel anisotropy $T_{\parallel} > T_{\perp}$ (as highlighted in the third panel of Figure 1, top) and intense wave activity at about the ion-cyclotron frequency, as revealed by the magnetic helicity (Pecora et al. 2021; Bowen et al. 2022; Trotta et al. 2024) in the bottom panel of the top window in Figure 1. The resonant interaction between these waves, belonging to the fast magnetosonic/whistler branch, and the proton beam is likely the cause of the hammerhead distributions (Verniero et al. 2022).

In the *turbulent stream* no hammerhead distributions are present (Figure 2, bottom) and the temperature anisotropy is less pronounced. No distinct wave activity is observed in this stream. However, the lack of wave activity could also be due either to the wave polarization plane not being properly sampled or to stronger turbulent fluctuations when θ_{BV} is perpendicular (Bowen et al. 2020b).

The spectral properties of the two streams are highlighted in Figure 3. Since solar wind turbulence is anisotropic with respect to the ambient magnetic field, we expect the sampling direction to affect the fluctuations spectral properties (Shebalin et al. 1983; Horbury et al. 2008; Podesta 2009; Chen et al. 2010; Horbury et al. 2012; Chen 2016; Bowen et al. 2020b; Sioulas et al. 2023). The top panel of Figure 3 shows the magnetic power spectral trace for the two intervals (black for the *wave stream*, red for the *turbulent stream*). The SCaM dataset is used for the former to avoid the flattening of the spectrum at high frequency present in the MAG data due to a low signal-to-noise ratio. The flattening is absent in the *turbulent stream* for which we use the MAG data. Vertical dashed lines show the ion-cyclotron frequency for the two streams (same colors), while reference power laws are indicated in gray.

The *wave stream* shows a steeper exponent of the power-spectral density (PSD) of the magnetic field fluctuations, compatible with -2, compared to the *turbulent stream* for which the spectral exponent is $-3/2$ (e.g., Boldyrev 2005, 2006). To be more precise for the former the linear regression in the log-log space gives a slope of -2.17 ± 0.05 in the range $[0.1, 0.9]$ Hz while for the latter -1.50 ± 0.01 in the range $[0.1, 4]$ Hz. The spectral slope difference could be attributed to different factors: i) the different sampling angle which makes sampling either quasi-perpendicular or quasi-parallel; ii) the different amplitude-to-ordered magnetic field which may induce a different type of turbulence (weak vs strong) in the two intervals (Meyrand et al. 2015), and iii) the spectral anisotropy which could steepen magnetic field spectra in the parallel direction (Schekochihin 2022). We also highlight that previous observations found evidence of a clear -2 spectrum at 1 au only if calculated with respect to the local mean field (Chen et al. 2011). Here, we observe a similar slope, despite we adopt the global mean field, since $B_{\rm rms}/\langle B\rangle$ is small (Table 1) and local- and global-mean field based analyses are expected to approach each other.

Notably, the *wave stream* PSD presents a substantial bump around the ion-cyclotron frequency (dashed black line in the top panel of Fig. 3) in agreement with the magnetic helicity signature in Fig. 1 (left).

The intermittency properties of the two intervals are evaluated using the scaling of the kurtosis, $K(\Delta t) = \langle \Delta \mathbf{B}(t)^4\rangle / \langle \Delta \mathbf{B}(t)^2\rangle^2 \sim \Delta t^{-\kappa}$, defined as the scale-dependent fourth-order moment of the distribution of the magnetic field fluctuations with Δt defining a time scale, normalized to the squared second-order moment (Frisch 1995; Bruno et al. 2003). The kurtosis is a measure of how fast the fluctuations distribution function tails go to zero, which is sensitive to how space filling the fluctuations at a given scale are. An increase in K toward smaller scales indicates higher distribution tails, so that the turbulent structures become confined to a progressively smaller fraction of space as the scale decreases. Consequently, intermittency in a generic time series manifests as a monotonic (power-law) increase of the kurtosis with decreasing scale (Frisch 1995; Sioulas et al. 2022; Mondal et al. 2025).

In order to evaluate $\mathbf{\Delta B}$ we use the 5 points increments method

$$\Delta \mathbf{B}(t, \Delta t) = \frac{1}{\sqrt{35}} \big[\mathbf{B}(t - 2\Delta t) - 4\mathbf{B}(t - \Delta t) + 6\mathbf{B}(t) - 4\mathbf{B}(t + \Delta t) + \mathbf{B}(t + 2\Delta t)\big]$$

which is more suitable for small scale increments since it can capture the proper scaling even when the spectrum is very steep (like in the transition range), contrary to the 2-points method (Cerri et al. 2019; Cho 2019; Sioulas et al. 2024).

The kurtosis is first computed for each magnetic field component, and then averaged (Sorriso-Valvo et al. 2023), to provide an overall indication of intermittency. As illustrated in the center panel of Figure 3, the kurtosis decreases as a power law of the time scale, confirming that a turbulent cascade is active in both streams (Frisch 1995). The scaling exponent is roughly -0.2, comparable to typical values in the solar wind (Sorriso-Valvo et al. 2023), and indicating strong intermittency. However, like for the magnetic power spectra, the kurtosis values are different in the two intervals. The larger K observed at all scales for the *turbulent stream* (red line) compared to the *wave stream* (black line) are indicative of enhanced intermittent fluctuations (i.e., with more non-Gaussian distributions) . Additionally, while in the *turbulent stream* the kurtosis flattens when approaching ion scales, the evident decrease in the *wave stream* suggests that the observed waves decorrelate the turbulent strucutures, restoring the Gaussian statistic of the fluctuations and thus eliminating the intermittency. Indeed a negative correlation between the presence of ion cyclotron wave activity and the level of intermittency has been observed also in Solar Orbiter data (Carbone et al. 2021).

The Hermite decomposition, described in Section 2, is applied to each VDF in the streams and the corresponding spectra, averaged over the full length of the intervals, are shown in the bottom panel of Figure 3. The oscillatory behavior in both spectra is due to the lack of power in the odd modes of the perpendicular spectrum caused by the gyrotropy assumption, which obviously affect also the 1D isotropic spectrum. The statistical error, computed as the standard deviation of the mean at each m, is too small to be distinguishable from the spectra.

In the *wave stream*, the Hermite coefficients for $m = 1, 2, 3$ contain more power than in the turbulent case, due to the presence of the beam and hammerhead structure. Indeed, tests with synthetic data (not shown) illustrate that the presence of a dense beam at a few thermal speeds, and a much less dense beam at $\gtrsim 5$ thermal speeds provide power only to the first few Hermite modes. In contrast, the *turbulent stream* velocity distribution functions exhibit a more Maxwellian core and velocity-space distortions at diverse velocity scales. The more Maxwellian core implies that the coefficient $m = 0$ has a higher power, which is part of the reason for the observed differences between the two streams at low m.

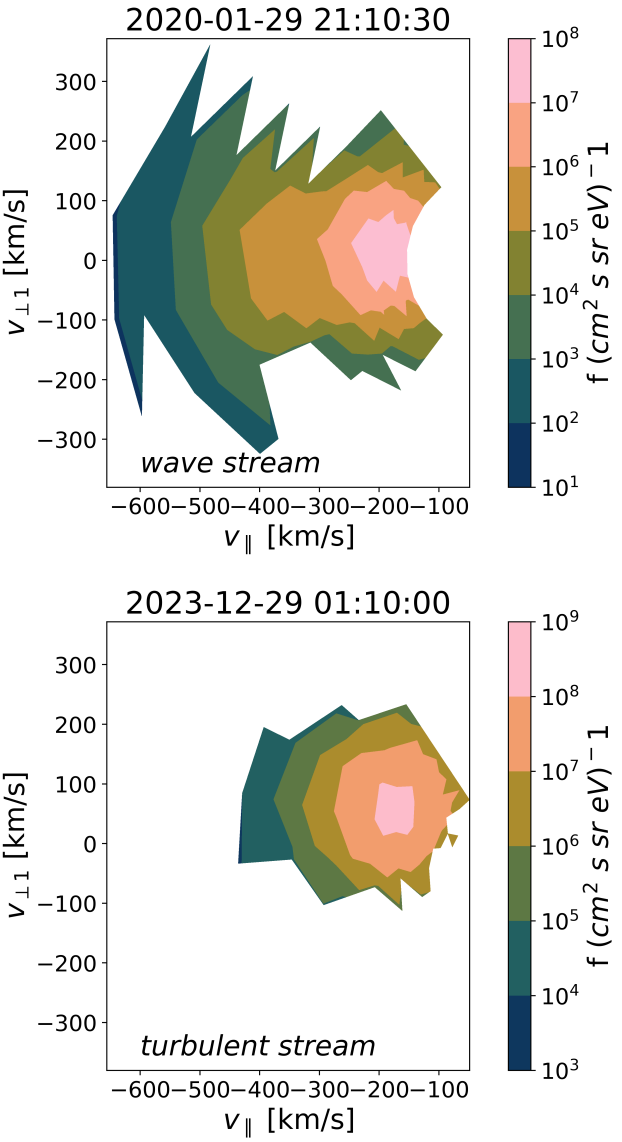


Figure 2. Representative VDFs for the *wave stream* (top) and *turbulent stream* (bottom). The VDFs are integrated along ϕ and plotted in the Energy-θ plane (see Verniero et al. 2020) in field aligned coordinates. These are the original non-gyrotropic PSP VDFs for which the procedure described in Sec 2 has not been applied yet.

Note that a similar behavior in the Hermite spectra for $1 \leq m \leq 4$ has been observed in Solar Orbiter data for the VDF of a reconnection exhaust with respect to the typical core-beam VDF of the ambient solar wind (Wu et al. 2023). At high m ($8 \lesssim m \lesssim 15$), the Hermite spectrum shows more power in the *turbulent stream* compared to the *wave stream*. This difference can be interpreted as an effect of the stronger velocity-space cascade in the *turbulent stream*, which induces fine-scale VDF distortions.

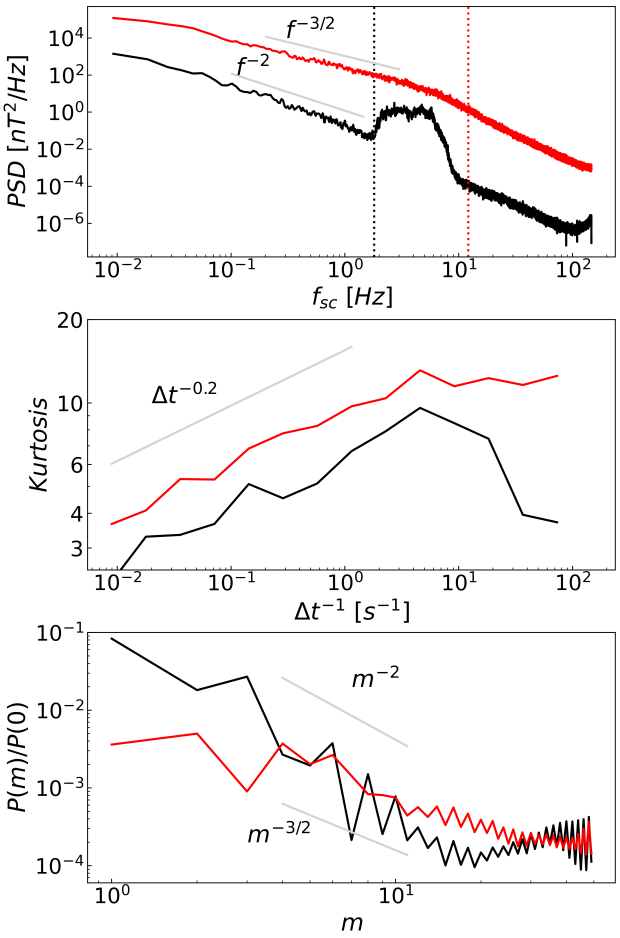


Figure 3. Top to bottom: Power spectral density and kurtosis of the magnetic field and average Hermite spectrum for the *wave stream* (black) and *turbulent stream* (red). In gray typical reference slopes (these are not fits) to aid the eye. The slopes for the Hermite spectra are the ones from the Servidio et al. (2017) phenomenological model.

The spectral slope computed in the range $4 \leq m < 12$, is about -2 for both streams. The range of m used to compute the Hermite spectral exponent is selected to ensure a sufficiently populated spherical shell while avoiding the high-m regime dominated by the noise. The slopes are consistent with the expectations for a low-β plasma (Servidio et al. 2017), but this agreement should be considered only qualitative considering the limitation imposed by the resolution of the instrument and the limited spectral range over which they are computed. Indeed the slope is very sensitive to the chosen range of m.

We tested the spectra against the ones built on the one-count VDFs and the spectra of bi-Maxwellian VDFs interpolated on SPAN grid. In both cases, the spectra in Figure 3 were above these signals interpreted as noise levels (see Appendix B). We purposefully did not discuss the spectra for $m \gtrsim 20$ because the flattening is likely due to the interpolation errors. This, however, does not affect Hermite modes at lower m.

4. TRANSFER AND CONVERSION OF ENERGY

In order to gain some insights on the ongoing energy transfer and dissipation, we compare the different field- and VDF-based diagnostics to highlight energy conversion (see, e.g., Pezzi et al. 2021, and references therein).

VDF-based proxies estimate how far the VDF is from the equilibrium Maxwellian distribution. Here, we adopt the Kauffman-Paterson measure (Kaufmann & Paterson 2009b; Liang et al. 2020)

$$M_{KP}(t) = \frac{s_M(t) - s(t)}{(3/2)k_B n}, \tag{6}$$

where $s(t) = -k_B \int d^3v f(\mathbf{v}, t) \ln f(\mathbf{v}, t)$ and n is the proton density, and the enstrophy (Servidio et al. 2017; Pezzi et al. 2018)

$$\Omega(t) = \sum_{m>0} [g_m(t)]^2. \tag{7}$$

The enstrophy is related to the Maxwellianity indicator $\epsilon = \frac{1}{n}\sqrt{\int (f - f_M)^2 d^3v}$ through $\Omega = \epsilon^2 n^2$, where f_M is the Maxwellian built using the local density and trace temperature (Pezzi et al. 2018).

The Kauffman-Paterson measure evaluate how far the entropy of the measured distribution $s(t)$ is from the entropy $s_M(t)$ of the local Maxwellian f_M. A value close to zero indicate that the plasma is close to local thermodynamical equilibrium (LTE) while, conversely, as this measure increases the plasma moves away from LTE. Note that M_{KP} is calculated on the original instrument grid, while the enstrophy Ω is calculated on the Hermite grid.

Field-based proxies generally estimate the energy available for energy conversion. Here, we consider the Local Energy Transfer (LET) (Sorriso-Valvo et al. 2015; Sorriso-Valvo et al. 2018, 2019; Marino & Sorriso-Valvo 2023), which provides an approximated estimate of the local (in time t and scale Δt) turbulent energy transfer,

$$\epsilon^{\pm}(t, \Delta t) = -\frac{3}{4} \frac{\Delta v_l (|\Delta \mathbf{v}|^2 + |\Delta \mathbf{b}|^2) - 2\Delta b_l (\Delta \mathbf{v} \cdot \Delta \mathbf{b})}{\Delta t \langle v \rangle}, \tag{8}$$

where Δv_l, $\Delta \mathbf{v}$, $\Delta \mathbf{b}$ are, respectively, the longitudinal velocity increments, the velocity and magnetic field increments computed with a lag Δt equal to the SPAN-i cadence. Moreover, we adopt the partial variance of increments estimating the strength of magnetic field gradients (Greco et al. 2008)

$$\mathrm{PVI} = \frac{|\Delta \mathbf{b}|^2}{\langle |\Delta \mathbf{b}|^2 \rangle}, \tag{9}$$

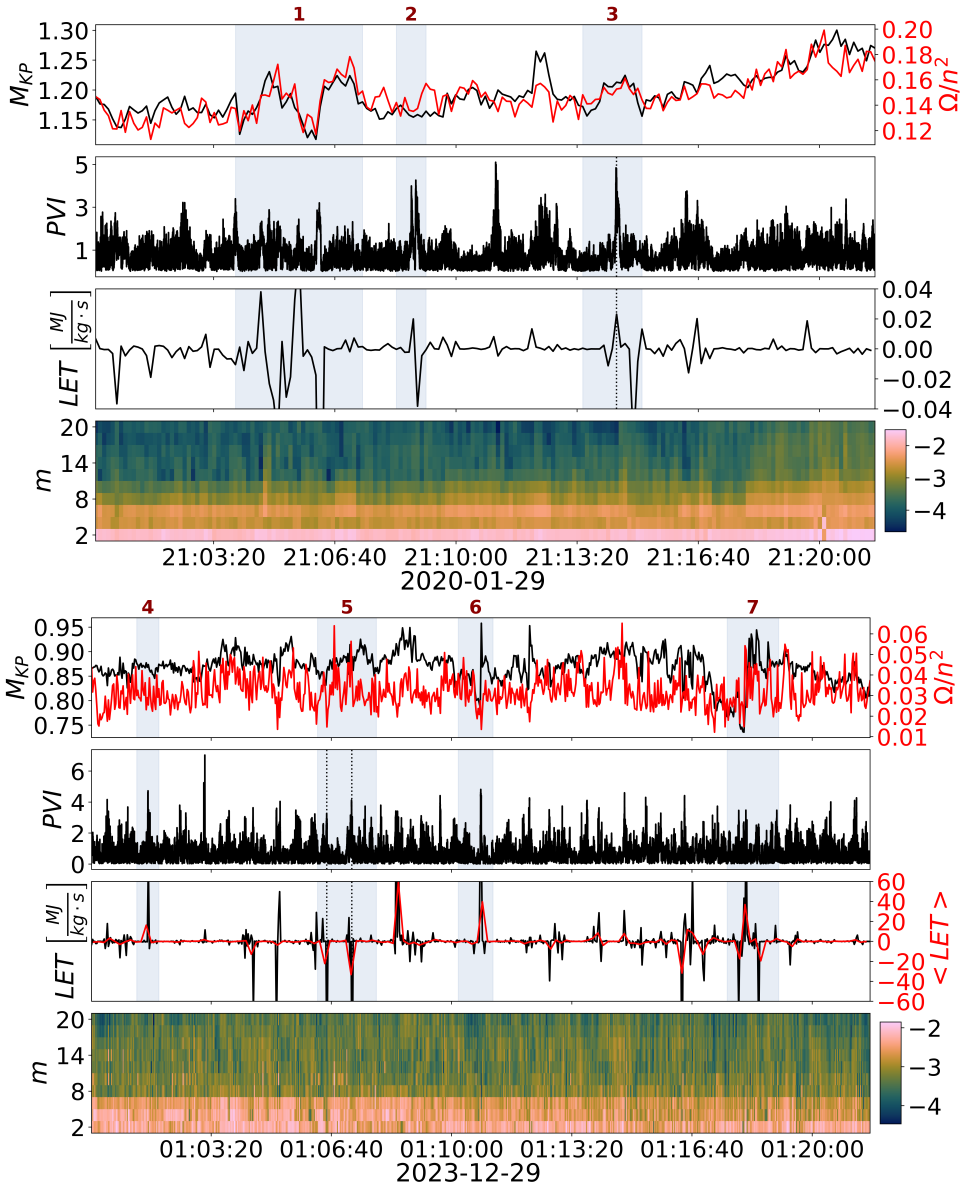


Figure 4. From top to bottom: Kaufman-Paterson measure and normalized enstrophy, PVI, LET, and Hermite spectrogram for the *wave stream* (top) and the *turbulent stream* (bottom). The shaded areas highlight regions of interest described in the main text. The Hermite spectrograms are represented through the scientifically derived color map batlow (Crameri et al. 2020).

where the increments are computed with a lag equal to the SPAN-i cadence, but on the much higher cadence MAG data. The lag choice is motivated by the idea of having for each VDF an associated value of the LET and to have a measure of the field gradients, through the PVI, on the same time scale at which the VDF is sampled. For both PVI and LET we use the standard 2-point increments, since at the scale of interest is at the bottom of the Kolmogorov range, where the spectra are not as steep as to require the more refined 5-point technique(Cerri et al. 2019).

Fig. 4 shows these quantities for the *wave stream* (top) and the *turbulent stream* (bottom). A good qualitative agreement between M_{KP} and Ω/n^2 (enstrophy normalized to the average stream density) is found for both streams (top panels), even though the two quantities are computed on different grids. This again supports the robustness of the analysis. Indeed, while the two measures are not formally identical, they both quantify deviations from Maxwellianity (Pezzi et al. 2021). The cause of the better agreement for the *wave stream* with respect to *turbulent stream* remains to be clarified.

Establishing quantitative correlations between energy conversion and dissipation variables in turbulent space plasmas is always complicated, since regional (adjacent peaks) rather than point-wise correlations naturally

arise (Servidio et al. 2017; Yang et al. 2019; Yordanova et al. 2021). In the two intervals analyzed here, we observe few instances in which the peaks or dips of PVI and enstrophy are simultaneous (the shaded areas numbered 3 and 5 in Fig. 4, with dotted lines to aid the eye), while the correspondence is generally more regional (as in the shaded area 2). Cases with no evident correlations also appear (e.g., shaded area 4).

A different argument holds for the LET variable. Indeed, LET peaks are much higher for the *turbulent stream*, as expected for a stream with perpendicular sampling and closer to the Sun. In both intervals, most of the LET peaks –indicative of enhanced turbulent energy transfer– are associated with peaks in M_{KP} and Ω (shaded areas 1, 3, 5, 6, 7). A similar behavior has been previously observed in Kelvin-Helmoltz vortices at the Earth magnetopause boundary layer (Sorriso-Valvo et al. 2019), where large values of the LET were found to be associated with either beams or broad energization in the VDFs, but not with more Maxwellian VDFs.

These results suggest that an enhanced nonlinear transfer in the real space affects the phase space too, in agreement with the concept of a dual real-velocity space cascade.

Finally we observe that the Hermite spectrogram (bottom panels of Fig 4) is more disturbed and rapidly fluctuating for the *turbulent stream* (confirming that the velocity-space cascade is intermittent (Pezzi et al. 2018)) while for the *wave stream* it is smoother and dominated by lower-m modes.

5. DISCUSSION AND CONCLUSION

In this letter, we investigate the Hermite decomposition of the gyrotropized Parker Solar Probe ion velocity distribution functions for two different streams, a super-Alfvénic stream at 28 $R_\odot$ and a sub-Alfvénic 11 $R_\odot$, referred to respectively as the *wave stream* and *turbulent stream*.

The streams under exam present similar level of fluctuations with respect to the background flow, a significant level of correlations between the velocity and magnetic field (high cross-helicity) but different β_p, angle to flow and velocity distribution functions shapes. The stream at $R \approx 28 R_{sun}$ presents coherent wave activity around the ion-cyclotron frequency and hammerhead distributions (Verniero et al. 2020, 2022), while in the stream at $R \approx 11 R_{sun}$, where the sampling is rather perpendicular ($\theta_{BV} = 116^\circ \pm 7^\circ$), the hammerhead features are not present.

These differences have a significant impact on the average Hermite spectrum and spectrogram. For the *wave stream* the Hermite spectrum is dominated by the first few modes, while for the *turbulent stream*, closer in, the higher order modes have relatively more power and the Hermite spectrogram is more intermittent. We speculate that this effect is related to (i) the presence of stronger turbulent fluctuations that, in turn, transfer more power to higher Hermite modes and, (ii) to the different sampling direction. The precise details of this mechanism must be investigated further. However, numerical efforts have provided compelling evidence for the ability of turbulence to transfer power to higher Hermite modes (Pezzi et al. 2018).

Furthermore, we study the behavior of different energization and dissipation proxies for the two streams. Although, at variance with previous works (Servidio et al. 2017; Pezzi et al. 2018), we do not observe a significant correlation between the enstrophy and the partial variance of increments of the magnetic field, our comparison of field-based (partial variance of increments and local energy transfer) and VDF-based (Kauffman-Paterson and the enstrophy) diagnostics reveals that there is good qualitative correlation between the peaks in local energy transfer and the ones in the Enstrophy and in the Kauffman-Paterson measures. These results support the idea that the turbulent cascade in nearly-reversible space and astrophysical plasmas is a *dual* cascade, influencing both real and velocity space (Schekochihin et al. 2008; Servidio et al. 2017; Cerri et al. 2018; Pezzi et al. 2018) and are important with respect to the long-standing problem of how heating and dissipation happen in collisionless plasma. Indeed, the preliminary evidence of the presence of a phase-space cascade in the inner heliosphere corroborates the argument that fine velocity distribution features can be crucial in irreversibly dissipating turbulent energy even when the collisional frequency is small (Schekochihin et al. 2008; Pezzi et al. 2016).

Future efforts will complement this analysis adopting different in-situ missions, such as Solar Orbiter, and in the context of existent and future multi-spacecraft missions (MMS, Helioswarm, and Plasma Observatory). Novel methods to reconstruct the velocity distribution functions, such as the one based on the Slepian function (Bharati Das & Terres 2025), will also be considered since they have the potential to improve the study of the phase-space cascade.

We thank C. H. K. Chen, M. Terres, J. Coburn, D. Manzini and S.S. Cerri for useful discussions. This research was preliminary discussed within (a) the ISSI International Team Project 23-588 ("Unveiling Energy Conversion and Dissipation in Non-Equilibrium Space Plasmas"), and (b) the International Exchanges Cost Share scheme/Joint Bilateral Agreement project "Multiscale electrostatic energisation of plasmas: comparison of collective processes in laboratory and space" funded by the Royal Society (UK) and the Consiglio Nazionale delle Ricerche (Italy) (award numbers IEC\R2\222050 and SAC.AD002.043.021). OP, DP, FV, LSV, and FP acknowledge the support of the PRIN 2022 project "2022KL38BK - The ULtimate fate of TuRbulence from space to laboratory plAsmas (ULTRA)" (Master CUP B53D23004850006) by the Italian Ministry of University and Research, funded under the National Recovery and Resilience Plan (NRRP), Mission 4 – Component C2 – Investment 1.1, "Fondo per il Programma Nazionale di Ricerca e Progetti di Rilevante Interesse Nazionale (PRIN 2022)" (PE9) by the European Union – NextGenerationEU. LSV was supported by the Swedish Research Council (VR) Research Grant N. 2022-03352. AL, LSV and FP acknowledge the project "Data-based predictions of solar energetic particle arrival to the Earth: ensuring space data and technology integrity from hazardous solar activity events" (CUP H53D23011020001) 'Finanziato dall'Unione europea - Next Generation EU' PIANO NAZIONALE DI RIPRESA E RESILIENZA (PNRR) Missione 4 "Istruzione e Ricerca" - Componente C2 Investimento 1.1, "Fondo per il Programma Nazionale di Ricerca e Progetti di Rilevante Interesse Nazionale (PRIN)" Settore PE09.

FP and AL acknowledges support from the Research Foundation – Flanders (FWO) Junior research project on fundamental research G020224N.

FV received funding from the European Union's Horizon Europe research and innovation program under Grant Agreement No. 101082633421 - AutomaticS in spAce exPloration (ASAP).

S. S. acknowledges the Space It Up project funded by the Italian Space Agency, ASI, and the Ministry of University and Research, MUR, under contract n. 2024-5-E.0 - CUP n. I53D24000060005

Software: MHDTurbPy (see the function TurbPy.flucts to compute increments and TurbPy.remove_wheel_noise to remove the reaction wheel peaks from the magnetic field spectrum) (Sioulas 2023), PySpedas **(Angelopoulos et al. 2019)**, PyUltra (https://github.com/orestepezzi/), PyPesto (currently under development) .

APPENDIX

A. GYROTROPIZATION OF THE VELOCITY DISTRIBUTION FUNCTION

The aim of this section is to give more details on the preprocessing and gyrotropization of VDFs briefly discussed in Sec 2. In Fig 5 we plot the same distribution function of Fig 2 (top) in FAC integrated along ϕ and plotted in the Energy-θ plane (left), integrated along θ and plotted in the Energy-ϕ plane (center) and its gyrotropized version following Bowen et al. (2022). θ and ϕ are respectevely the elevation and azimuthal angle of SPANi (Livi et al. 2022). The VDFs are centered by subtracting the bulk speed.

The limited field of view due to the heat shield is visible in the Energy-ϕ plane (center). The rightmost panel shows the full VDF (not integrated along any direction) collapsed in the new grid where $v_\parallel$ is unchanged and $v_\perp = \sqrt{v_{\perp 1}^2 + v_{\perp 2}^2}$, extended to the $-v_\perp$ by imposing $f(-v_\perp) = f(v_\perp)$. The Hermite transform is performed on the latter VDF, once the grid has been normalized to the parallel and perpendicular thermal speeds and interpolated onto the Hermite grid.

This procedure provides a reduced distribution function that accurately represents the PSP measurements while mitigating the effects of FOV limitations.

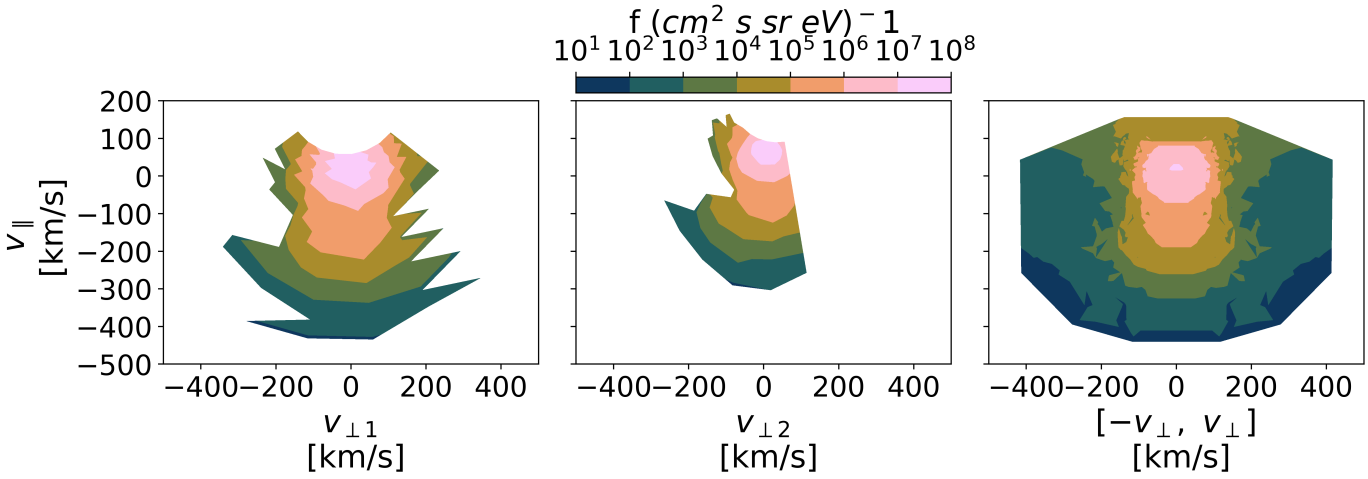


Figure 5. VDF processing for the *wave stream*. VDF averaged over ϕ and plotted in the Energy-θ plane (left), VDF averaged over θ and plotted in the Energy-ϕ plane (center), VDF after the procedure describer in Sec 2 before the interpolation into the Hermite Grid.

B. HERMITE SPECTRA: DATA VS BI-MAXWELLIANS

In order to evaluate whether the Hermite spectra shown in Fig 3 are meaningful we perform the same analysis on bi-Maxwellian distributions obtained from the density and parallel and perpendicular temperature of each measurements in the two streams. For each bi-Maxwellian, we compute the Hermite spectrum and we then average to obtain the spectra shown in Fig 6.

The purpose of the comparison in Fig. 6 is to demonstrate that the measured spectra are meaningful: the observed signal lies above that of the underlying bi-Maxwellians, which can be considered the lowest-order non-trivial VDF against which to benchmark our spectra. The spectra are also above the one count noise level (not shown).

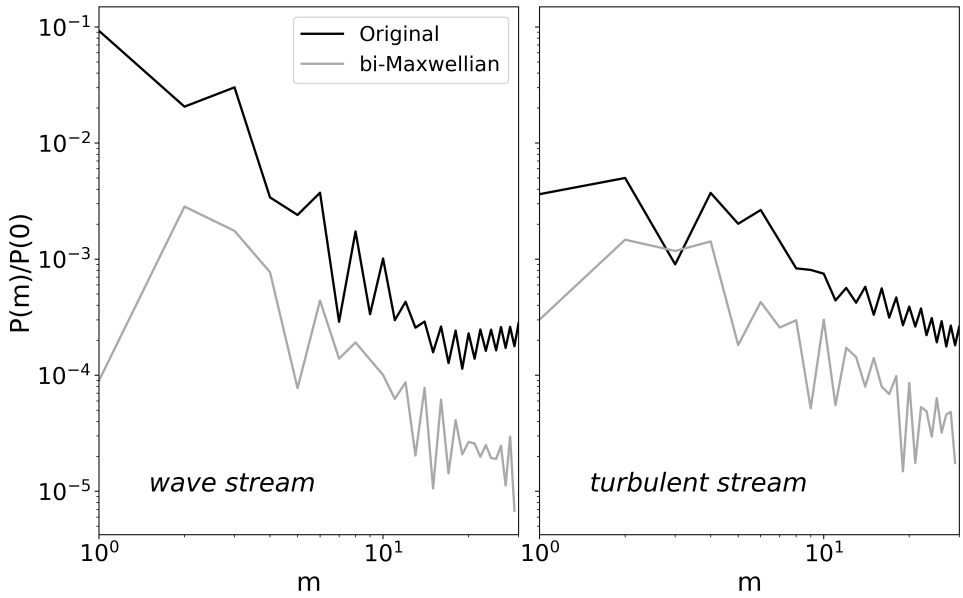


Figure 6. Original Hermite spectrum for the *wave stream* (left) and *turbulent stream* (right) in black compared with the Hermite spectrum of the underlying bi-Maxwellian in gray.

REFERENCES

Angelopoulos, V., Cruce, P., Drozdov, A., et al. 2019, SSRv, 215, 9, doi: 10.1007/s11214-018-0576-4

Bale, S. D., Goetz, K., Harvey, P. R., et al. 2016, SSRv, 204, 49, doi: 10.1007/s11214-016-0244-5

Bharati Das, S., & Terres, M. 2025, ApJ, 982, 96, doi: 10.3847/1538-4357/adb6a0

Boldyrev, S. 2005, ApJL, 626, L37, doi: 10.1086/431649

—. 2006, PhRvL, 96, 115002, doi: 10.1103/PhysRevLett.96.115002

Bowen, T. A., Bale, S. D., Bonnell, J. W., et al. 2020a, Journal of Geophysical Research (Space Physics), 125, e27813, doi: 10.1029/2020JA027813

Bowen, T. A., Mallet, A., Huang, J., et al. 2020b, ApJS, 246, 66, doi: 10.3847/1538-4365/ab6c65

Bowen, T. A., Chandran, B. D. G., Squire, J., et al. 2022, PhRvL, 129, 165101, doi: 10.1103/PhysRevLett.129.165101

Bruno, R., & Carbone, V. 2013, Living Reviews in Solar Physics, 10, 2, doi: 10.12942/lrsp-2013-2

Bruno, R., Carbone, V., Sorriso-Valvo, L., & Bavassano, B. 2003, J. of Geophys. Res.: Space Phys., 108, 1130

Carbone, F., Sorriso-Valvo, L., Khotyaintsev, Y. V., et al. 2021, A&A, 656, A16, doi: 10.1051/0004-6361/202140931

Cassak, P. A., Barbhuiya, M. H., Liang, H., & Argall, M. R. 2023, PhRvL, 130, 085201, doi: 10.1103/PhysRevLett.130.085201

Celebre, G., Servidio, S., & Valentini, F. 2023, Physics of Plasmas, 30, 092304, doi: 10.1063/5.0160549

Cerri, S. S., Arzamasskiy, L., & Kunz, M. W. 2021, ApJ, 916, 120, doi: 10.3847/1538-4357/abfbde

Cerri, S. S., Grošelj, D., & Franci, L. 2019, Frontiers in Astronomy and Space Sciences, 6, 64, doi: 10.3389/fspas.2019.00064

Cerri, S. S., Kunz, M. W., & Califano, F. 2018, ApJL, 856, L13, doi: 10.3847/2041-8213/aab557

Chen, C. H. K. 2016, Journal of Plasma Physics, 82, 535820602, doi: 10.1017/S0022377816001124

Chen, C. H. K., Mallet, A., Yousef, T. A., Schekochihin, A. A., & Horbury, T. S. 2011, MNRAS, 415, 3219, doi: 10.1111/j.1365-2966.2011.18933.x

Chen, C. H. K., Wicks, R. T., Horbury, T. S., & Schekochihin, A. A. 2010, ApJL, 711, L79, doi: 10.1088/2041-8205/711/2/L79

Cho, J. 2019, ApJ, 874, 75, doi: 10.3847/1538-4357/ab06f3

Coburn, J. T., Verscharen, D., Owen, C. J., et al. 2024, ApJ, 964, 100, doi: 10.3847/1538-4357/ad1329

Crameri, F., Shephard, G. E., & Heron, P. J. 2020, Nature Communications, 11, 5444, doi: 10.1038/s41467-020-19160-7

Dudok de Wit, T., Krasnoselskikh, V. V., Agapitov, O., et al. 2022, Journal of Geophysical Research (Space Physics), 127, e30018, doi: 10.1029/2021JA030018

Fox, N. J., Velli, M. C., Bale, S. D., et al. 2016, SSRv, 204, 7, doi: 10.1007/s11214-015-0211-6

Frisch, U. 1995, Turbulence: The Legacy of A.N. Kolmogorov (Cambridge University Press)

Greco, A., Chuychai, P., Matthaeus, W. H., Servidio, S., & Dmitruk, P. 2008, Geophys. Res. Lett., 35, L19111, doi: 10.1029/2008GL035454

Horbury, T. S., Forman, M., & Oughton, S. 2008, PhRvL, 101, 175005, doi: 10.1103/PhysRevLett.101.175005

Horbury, T. S., Wicks, R. T., & Chen, C. H. K. 2012, SSRv, 172, 325, doi: 10.1007/s11214-011-9821-9

Howes, G. G. 2018, Physics of Plasmas, 25, 055501, doi: 10.1063/1.5025421

Huang, R., Howes, G. G., & McCubbin, A. J. 2024, Journal of Plasma Physics, 90, 535900401, doi: 10.1017/S0022377824000667

Jannet, G., Dudok de Wit, T., Krasnoselskikh, V., et al. 2021, Journal of Geophysical Research (Space Physics), 126, e28543, doi: 10.1029/2020JA028543

Kasper, J. C., Abiad, R., Austin, G., et al. 2016, SSRv, 204, 131, doi: 10.1007/s11214-015-0206-3

Kaufmann, R. L., & Paterson, W. R. 2009a, Journal of Geophysical Research (Space Physics), 114, A00D04, doi: 10.1029/2008JA014030

—. 2009b, Journal of Geophysical Research (Space Physics), 114, A00D04, doi: 10.1029/2008JA014030

Klein, K. G., Perez, J. C., Verscharen, D., Mallet, A., & Chandran, B. D. G. 2015, ApJL, 801, L18, doi: 10.1088/2041-8205/801/1/L18

Liang, H., Barbhuiya, M. H., Cassak, P. A., et al. 2020, Journal of Plasma Physics, 86, 825860502, doi: 10.1017/S0022377820001270

Livi, R., Larson, D. E., Kasper, J. C., et al. 2022, ApJ, 938, 138, doi: 10.3847/1538-4357/ac93f5

Marino, R., & Sorriso-Valvo, L. 2023, PhR, 1006, 1, doi: 10.1016/j.physrep.2022.12.001

Matthaeus, W. H., Goldstein, M. L., & Smith, C. 1982, PhRvL, 48, 1256, doi: 10.1103/PhysRevLett.48.1256

Meyrand, R., Kiyani, K. H., & Galtier, S. 2015, Journal of Fluid Mechanics, 770, R1, doi: 10.1017/jfm.2015.141

Mondal, S., Banerjee, S., & Sorriso-Valvo, L. 2025, The Astrophysical Journal, 982, 199, doi: 10.3847/1538-4357/adba54

Nastac, M. L., Ewart, R. J., Sengupta, W., et al. 2024, PhRvE, 109, 065210, doi: 10.1103/PhysRevE.109.065210

Owens, M. J., & Forsyth, R. J. 2013, Living Reviews in Solar Physics, 10, 5, doi: 10.12942/lrsp-2013-5

Parker, J. T., Highcock, E. G., Schekochihin, A. A., & Dellar, P. J. 2016, Physics of Plasmas, 23, 070703, doi: 10.1063/1.4958954

Pecora, F., Servidio, S., Greco, A., & Matthaeus, W. H. 2021, A&A, 650, A20, doi: 10.1051/0004-6361/202039639

Pezzi, O., Perrone, D., Servidio, S., et al. 2019, ApJ, 887, 208, doi: 10.3847/1538-4357/ab5285

Pezzi, O., Servidio, S., Perrone, D., et al. 2018, Physics of Plasmas, 25, 060704, doi: 10.1063/1.5027685

Pezzi, O., Valentini, F., & Veltri, P. 2016, PhRvL, 116, 145001, doi: 10.1103/PhysRevLett.116.145001

Pezzi, O., Liang, H., Juno, J. L., et al. 2021, MNRAS, 505, 4857, doi: 10.1093/mnras/stab1516

Podesta, J. J. 2009, ApJ, 698, 986, doi: 10.1088/0004-637X/698/2/986

Raouafi, N. E., Matteini, L., Squire, J., et al. 2023, SSRv, 219, 8, doi: 10.1007/s11214-023-00952-4

Schekochihin, A. A. 2022, Journal of Plasma Physics, 88, 155880501, doi: 10.1017/S0022377822000721

Schekochihin, A. A., Cowley, S. C., Dorland, W., et al. 2008, Plasma Physics and Controlled Fusion, 50, 124024, doi: 10.1088/0741-3335/50/12/124024

Schekochihin, A. A., Parker, J. T., Highcock, E. G., et al. 2016, Journal of Plasma Physics, 82, 905820212, doi: 10.1017/S0022377816000374

Servidio, S., Chasapis, A., Matthaeus, W. H., et al. 2017, PhRvL, 119, 205101, doi: 10.1103/PhysRevLett.119.205101

Shebalin, J. V., Matthaeus, W. H., & Montgomery, D. 1983, Journal of Plasma Physics, 29, 525, doi: 10.1017/S0022377800000933

Sioulas, N. 2023, MHDTurbPy, 0.1.0, Zenodo, doi: 10.5281/zenodo.7572468

Sioulas, N., Huang, Z., Velli, M., et al. 2022, ApJ, 934, 143, doi: 10.3847/1538-4357/ac7aa2

Sioulas, N., Velli, M., Huang, Z., et al. 2023, ApJ, 951, 141, doi: 10.3847/1538-4357/acc658

Sioulas, N., Zikopoulos, T., Shi, C., et al. 2024, arXiv e-prints, arXiv:2404.04055, doi: 10.48550/arXiv.2404.04055

Sorriso-Valvo, L., Carbone, F., Perri, S., et al. 2018, SoPh, 293, 10, doi: 10.1007/s11207-017-1229-6

Sorriso-Valvo, L., Marino, R., Lijoi, L., Perri, S., & Carbone, V. 2015, ApJ, 807, 86, doi: 10.1088/0004-637x/807/1/86

Sorriso-Valvo, L., Marino, R., Foldes, R., et al. 2023, A&A, 672, A13, doi: 10.1051/0004-6361/202244889

Sorriso-Valvo, L., Catapano, F., Retinò, A., et al. 2019, PhRvL, 122, 035102, doi: 10.1103/PhysRevLett.122.035102

Tatsuno, T., Dorland, W., Schekochihin, A. A., et al. 2009, PhRvL, 103, 015003, doi: 10.1103/PhysRevLett.103.015003

Trotta, D., Larosa, A., Nicolaou, G., et al. 2024, ApJ, 962, 147, doi: 10.3847/1538-4357/ad187d

Verniero, J. L., Larson, D. E., Livi, R., et al. 2020, ApJS, 248, 5, doi: 10.3847/1538-4365/ab86af

Verniero, J. L., Chandran, B. D. G., Larson, D. E., et al. 2022, ApJ, 924, 112, doi: 10.3847/1538-4357/ac36d5

Whittlesey, P. L., Larson, D. E., Kasper, J. C., et al. 2020, ApJS, 246, 74, doi: 10.3847/1538-4365/ab7370

Wu, Z., He, J., Duan, D., et al. 2023, ApJ, 951, 98, doi: 10.3847/1538-4357/accf9b

Yang, Y., Wan, M., Matthaeus, W. H., et al. 2019, MNRAS, 482, 4933, doi: 10.1093/mnras/sty2977

Yordanova, E., Vörös, Z., Sorriso-Valvo, L., Dimmock, A. P., & Kilpua, E. 2021, ApJ, 921, 65, doi: 10.3847/1538-4357/ac1942